Acta Neuropathologica
Communications

Distinct characteristics of brain metastasis in lung adenocarcinoma: development of high-confidence cell lines

Jintao He[1], Zen-ichi Tanei[1,2*], Dao-Sian Wu[3], Lei Wang[1,4], Yoshitaka Oda[1,2], Masumi Tsuda[1,4] and Shinya Tanaka[1,2,4]

Abstract

Lung cancer is a leading cause of cancer-related deaths worldwide, with brain metastasis occurring in approximately 30–55% of patients, particularly in lung adenocarcinoma. Due to the challenges in obtaining genuine brain metastasis tumor cells, researchers commonly use nude mouse models to establish brain metastasis cell lines, though traditional methods have limitations such as high costs, lengthy timeframes, and the need for specialized imaging equipment. To address these issues, we developed an improved approach by performing low cell number circulating intracranial injections (500–4000 cells) in nude mice, successfully establishing the H1975-BM1, BM2, and BM3 cell lines. Through RNA sequencing and bioinformatics analyses, we identified transcriptomic differences among these cell lines, revealing that H1975-BM1 cells primarily exhibit stem cell function and migration characteristics, while H1975-BM3 cells display enhanced chemotaxis, cell adhesion, and cytokine secretion associated with interactions. Experimental validation, including Transwell assays, CCK8, cell adhesion assays, and subcutaneous tumor implantation in nude mice, further confirmed these findings, with H1975-BM3 forming larger tumors and a more pronounced secretion cystic cavity. In conclusion, our improved methodology successfully established high-confidence brain metastasis lung adenocarcinoma cell lines, elucidating distinct transcriptomic and functional characteristics at different stages of brain metastasis progression.

Keywords Lung adenocarcinoma, Brain metastasis, Cell lines, Transcriptomic analysis

*Correspondence:
Zen-ichi Tanei
tanei@med.hokudai.ac.jp
[1]Department of Cancer Pathology, Faculty of Medicine, Hokkaido University, Sapporo, Japan
[2]Department of Surgical Pathology, Hokkaido University Hospital, Sapporo, Japan
[3]School of Medicine, College of Medicine, Taipei Medical University, Taipei 110301, Taiwan ROC
[4]Institute for Chemical Reaction Design and Discovery (WPI-ICReDD), Hokkaido University, Sapporo, Japan

Introduction

Lung cancer is the leading cause of cancer incidence and mortality worldwide [4]. Lung adenocarcinoma (LUAD) is the most common subtype, accounting for approximately 40% of all lung cancer cases [29]. About 30–55% of lung cancer patients develop brain metastases (BM), with LUAD being a major contributor to BM occurrence [31]. Notably, LUAD patients with EGFR mutations have a higher risk of BM [9, 18].

In recent years, research on BM-LUAD has increased. However, due to the characteristics of BM tumors, many researchers face challenges in obtaining primary BM cells from patients. As a result, most studies rely on animal models to establish BM cell lines [27].

Existing methods for generating BM cell lines can be categorized into two main approaches. The first involves injecting luciferase-labeled LUAD cells into the left ventricle or carotid artery of nude mice [33]. BM formation is monitored using in vivo imaging, and once metastases develop, mice are sacrificed to extract tumor tissue for cell culture. This cycle is typically repeated three times to obtain BM cell lines with strong affinity for the brain microenvironment. While this approach yields reliable cell lines, it has several drawbacks. The procedure has a high mortality rate due to left ventricular or carotid artery injection, requires multiple mice per batch, and incurs high costs. Additionally, the process is time-consuming since BM formation and progression must be observed. The use of specialized imaging equipment further limits its widespread application [8, 13, 36].

The second approach is simpler, involving direct intracranial injection of LUAD cells into nude mice [10, 19, 25]. After tumor progression, mice are sacrificed, and tumor tissue is cultured for subsequent rounds of injection, typically repeated three times. This method is cost-effective and time-efficient. However, it has inherent limitations. In physiological BM development, only a small number of tumor cells (dozens to hundreds) successfully colonize the brain. In contrast, intracranial injection delivers a large number of tumor cells directly into the brain [10, 19], leading to rapid tumor growth that bypasses early metastatic processes. This prevents proper interaction between tumor cells and the brain microenvironment, potentially altering cellular characteristics. Consequently, BM cell lines generated by this method may lack full biological relevance.

To overcome these limitations, we developed an improved method for establishing BM-LUAD cell lines. Using bioinformatics analysis and experimental validation, we characterized BM-LUAD at different stages and demonstrated the high reliability of our new cell lines.

Materials and methods
Cell lines and culture
Considering that LUAD patients with EGFR mutations have a higher risk of BM, we selected the H1975 cell line—which carries an EGFR mutation and stably expresses luciferase—as our parental cell line. This cell line was obtained from the Japanese Collection of Research Bioresources Cell Bank (No. JCRB1486). Both H1975 and the BM cell lines derived later were cultured in RPMI-1640 medium (Nissui Pharmaceutical) supplemented with 10% fetal bovine serum (FBS; Sigma-Aldrich) and 1% penicillin-streptomycin. All cells were maintained in a humidified incubator at 37 °C with 5% CO_2. Cells were detached by gentle pipetting with a solution of 0.02% EDTA and 0.25% trypsin (Sigma-Aldrich),

then passaged or collected and counted for animal experiments.

Intracranial Injection
In this study, all animal experiments used female nude mice (BALB/cAJcl-nu/nu, 5- or 6-week-old) purchased from CLEA Japan, Inc. For intracranial injections, mice were first anesthetized with isoflurane. They were then secured in a stereotactic injection device and positioned under a microscope.

After disinfecting the skin with 70% ethanol, a small incision was made with fine scissors and forceps to separate the subcutaneous tissue and expose the bregma. Using a mouse brain atlas and the stereotactic device, the injection site was determined. A small animal dental drill was used carefully to create a hole in the skull; drilling was stopped immediately when a distinct gap was felt. The drill bit was disinfected beforehand, and the hole diameter did not exceed 1 mm.

Following drilling, a 10 μL syringe (Hamilton syringe 701 N 80300) was used to draw 10 μL of the prepared cell suspension. The suspension consisted of 8 μL of PBS containing tumor cells and 2 μL of Matrigel (Corning Matrigel Basement Membrane Matrix, 356234). Note that the time between cell suspension preparation and the start of the injection should not exceed 90 min to maintain cell viability.

The injection depth was adjusted using the stereotactic device, and an automatic injector completed the injection within 10 min. After the injection, the syringe was slowly withdrawn to avoid creating air bubbles. The scalp was then sutured with 6–0 suture, and the sutures were removed one week after surgery.

Beginning two weeks post-surgery, the mice were weighed daily. If a mouse lost more than 20% of its pre-operative body weight, it was considered to have reached an endpoint and was euthanized under isoflurane anesthesia.

After confirming death, tissue scissors were used to cut along the posterior region near the foramen magnum, separating the head from the body. An ophthalmic scissor then cut along the vertical midline between the eyes to expose the skull. A curved-tip scissor was carefully inserted into the sagittal suture and used to lever apart both sides of the skull, exposing the brain.

The brain was placed under the microscope, and a side-rounded micro knife was used to carefully separate the cerebral cortex at the injection area, exposing necrotic tumor tissue. The tumor tissue was excised with the micro knife and placed into a 15 mL centrifuge tube containing pre-chilled PBS.

The tube was centrifuged at 2000 rpm for 1 min, and the supernatant was discarded. Next, 3–4 mL of a solution containing 0.02% EDTA and 0.25% trypsin was

added, and the tumor tissue was gently pipetted with a 1000 µL pipette until no visible cell aggregates remained. Then, 10 mL of complete medium was added to stop the enzymatic digestion. After centrifuging at 3000 rpm for 2 min, the supernatant was discarded and the cell pellet was resuspended in an appropriate amount of complete medium. The cells were then plated for culture.

This process was repeated three times with injections of 500, 4000, and 4000 cells, respectively, to establish the H1975-BM1, H1975-BM2, and H1975-BM3 cell lines. For survival studies, the intracranial injection procedure was the same but the number of injected cells was 4000 in each case.

Left ventricular injection

Mice were anesthetized with isoflurane and placed in a supine position. The chest was disinfected with 70% ethanol, and the left ventricle was located by palpating the cardiac apex. A 29G syringe (TERUMO Co.) was then used to slowly inject 100 µL of cell suspension (containing 1×10^5 tumor cells in PBS) into the left ventricle at an angle of approximately 10–15°. After the injection, the mice were monitored as they recovered; if no abnormal behavior was observed, they were returned to normal housing.

Tumor growth and metastasis were monitored using the IVIS Lumina imaging system (PerkinElmer). Mice received an intraperitoneal injection of D-luciferin dissolved in PBS and were anesthetized with isoflurane. Five minutes post-injection, imaging was conducted with the settings: 5-minute exposure time, large binning, and an f-stop of 1. The mice were imaged weekly to track tumor progression.

Subcutaneous injection

Mice were anesthetized with inhaled isoflurane and positioned in a prone position. After disinfecting the back with 70% ethanol, the skin was gently lifted with forceps. Using a 10 µL syringe (Hamilton Syringe 701 N 80300), 10 µL of the prepared cell suspension (containing 1.2×10^5 tumor cells in PBS) was injected subcutaneously.

After 21 days, the mice were anesthetized and euthanized. Under a microscope, tumor tissue was carefully dissected using fine scissors and forceps, taking care to avoid rupturing any cystic compartments. The tissue was then fixed in 5% formalin and photographed. Using a reference scale, ImageJ software was employed to measure and calculate the total volume, tumor volume, and cyst volume, where the cyst volume was determined by subtracting the tumor volume from the total volume.

Cell migration

The migration capability of the cells was evaluated using a Transwell chamber assay. Two types of polycarbonate filter chambers were employed: one with 8 µm pores (Corning Transwell 3422) and another with 12 µm pores (Guangzhou Jet Bio-Filtration Co., TCS100024). Prior to the assay, cells were starved in a medium containing 1% FBS for 12 h to minimize the influence of FBS on migration. Then, 5×10^4 cells were resuspended in 200 µL of 1% FBS medium and seeded into the upper chamber of the Transwell. In the lower chamber, 600 µL of RPMI-1640 medium with 10% FBS was added as a chemoattractant. The cells were incubated at 37 °C in a 5% CO_2 atmosphere for 48 h. After incubation, the chambers were rinsed twice with PBS and fixed with 4% paraformaldehyde for 15 min. Non-migrated cells on the upper membrane surface were gently removed using a cotton swab, and the membranes were then stained with 0.1% crystal violet for 10 min. Finally, images were captured using an inverted microscope (Olympus IX73).

Cell adhesion

For the cell adhesion assay, ultra-low attachment microplates (Corning 24-well plate 3473) were used to prevent cells from adhering to the plate, while 1% FBS medium was employed to avoid interference from cell proliferation. A total of 1×10^4 cells were resuspended in 1 mL of 1% FBS medium and seeded into each well of a 24-well plate. Four cell lines—H1975, H1975-BM1, H1975-BM2, and H1975-BM3—were tested with six replicates for each line. The cells were incubated at 37 °C with 5% CO_2 for 24 h. After incubation, the cell clusters were observed and photographed under an inverted microscope (Olympus IX73). Using a reference scale, ImageJ was then applied to measure and calculate the major axis of the cell clusters.

Cell proliferation assay

Cell proliferation was measured using the Cell Counting Kit-8 (CCK-8) assay. Briefly, cells were seeded in 96-well plates at a density of 5,000 cells per well. At specified time points, 10 µL of the CCK-8 reagent (Dojindo Laboratories, CK04) was added to each well and the plates were incubated according to the manufacturer's protocol. The absorbance at 450 nm was then recorded using a microplate reader (Thermo Scientific Multiskan FC) to evaluate cell viability and proliferation.

RNA extraction and bulk RNA sequencing

RNA was extracted from four cell lines (H1975, H1975-BM1, H1975-BM2, and H1975-BM3) following the standard protocol of the RNeasy Mini Kit (Qiagen). Three independent samples were prepared for each cell line. The RNA samples were then sent to BGI's Japan branch for sequencing on the DNBSEQ platform (PE150, 6G data per sample). All samples were sequenced simultaneously to avoid batch effects. After obtaining the

FASTQ files, the data were cleaned using fastp [5]. Using GRCh38 as the reference genome, the Salmon pipeline [23] generated Count and TPM (Transcripts Per Kilobase Million) matrices for further analysis.

Single-cell RNA sequencing analysis

We selected the GSE131907 dataset from the GEO database for analysis and used only the primary LUAD and BM-LUAD samples [14]. Downstream analysis was performed in R using Seurat V5 [12]. Cells were included if they had between 300 and 7000 genes, a mitochondrial gene percentage below 10%, and total counts below 40,000. The top 2000 most variable genes were selected as highly variable genes. Sample integration was performed with the CCA algorithm using 3000 anchors. Dimensionality reduction and clustering were carried out using PCA (PCs 1–40) at a resolution of 0.1. Marker genes were calculated with the COSGR package [7], and cell types were manually annotated based on these markers. Ten major cell types were identified, with both epithelial and cycling epithelial cells classified as tumor cells.

To further investigate tumor cell subpopulations, we extracted the UMI count expression matrix for tumor cells and repeated the downstream analysis. Again, the top 2000 most variable genes were chosen as highly variable genes. This time, sample integration was performed with the CCA algorithm using 2000 anchors, followed by PCA (PCs 1–40) at a resolution of 0.2. All tumor cells were then subdivided into six subpopulations, named Tumor C0 to Tumor C5.

As all tumor cells came from two groups (primary LUAD and BM-LUAD), we evaluated the distribution tendency of tumor cell subpopulations between these groups using the Ro/e index (the ratio of observed over expected cell numbers) [39]. This method removes the bias from differences in total cell numbers and allows for direct comparison of subpopulation enrichment. Based on the Ro/e values (+++ for Ro/e > 1.2; ++ for $1 < \text{Ro/e} \leq 1.2$; + for $0.6 \leq \text{Ro/e} \leq 1$; +/− for $0 < \text{Ro/e} < 0.6$), Tumor C0, Tumor C1, and Tumor C3 were found to be more enriched in BM samples.

Similarity analysis

Due to current technical limitations, scRNA-seq data for tumor cells often contain significant noise. To reduce the impact of noise on downstream analysis, we used the Metacell algorithm [3] to merge 30 similar tumor cells into one metacell, thereby creating a metacell matrix [6]. Next, we used the R package IOBR [38] and the metacell matrix as a reference. Based on the CIBERSORT algorithm [22], we deconvolved the bulk RNA-seq data from our BM cell line. This allowed us to analyze the proportions of different tumor cell subpopulations in the BM

cell line and assess their similarity to actual BM tumor cells.

WGCNA analysis

We used the weighted gene co-expression network analysis (WGCNA) method [16] to systematically explore gene co-expression patterns and their relationship with different stages of the BM cell lines [37]. First, we used the TPM matrix and retained 8965 genes that showed differences between groups ($P < 0.05$) to ensure high-quality and stable data. Next, we calculated the Pearson correlation coefficients for all gene pairs to build a correlation matrix. Based on the scale-free topology criterion, we selected a soft threshold (softPower = 9) to convert the correlation matrix into a weighted adjacency matrix, making the network more consistent with biology. Then, we computed the topological overlap matrix (TOM) from the weighted adjacency matrix. The TOM not only considers the direct correlations between genes but also reflects the shared neighbors, providing a robust distance measure for subsequent hierarchical clustering. Using the distance matrix (1−TOM), we applied the dynamic tree cutting algorithm to group genes with similar expression patterns into co-expression modules. Modules with high similarity were further merged based on the first principal component of gene expression (module eigengene) to obtain biologically meaningful modules. Finally, we calculated the Pearson correlation coefficients between the module eigengenes and the different stages of the BM cell lines. Modules that showed significant associations were then subjected to gene ontology (GO) functional enrichment analysis to reveal their potential biological functions and regulatory mechanisms.

Statistical analysis

Unless noted otherwise, all experiments were conducted in triplicate. Results are expressed as mean ± standard deviation (SD). We used Student's t-test or one-way ANOVA with Tukey's post hoc test to assess statistical significance. Survival data were analyzed with Kaplan-Meier curves, and groups were compared using log-rank tests. A p-value of less than 0.05 was considered statistically significant.

Results

Intracranial serial injection and brain metastatic potential validation

We used the H1975 cell line, which stably expresses luciferase, as the parental cell line. To establish brain metastasis (BM) cell lines, we performed serial intracranial injections of a low number of tumor cells into the hippocampal region of nude mice (Fig. 1A, B). As the tumors progressed, mice exhibited gradual weight loss, and those with a weight reduction exceeding 20% were considered
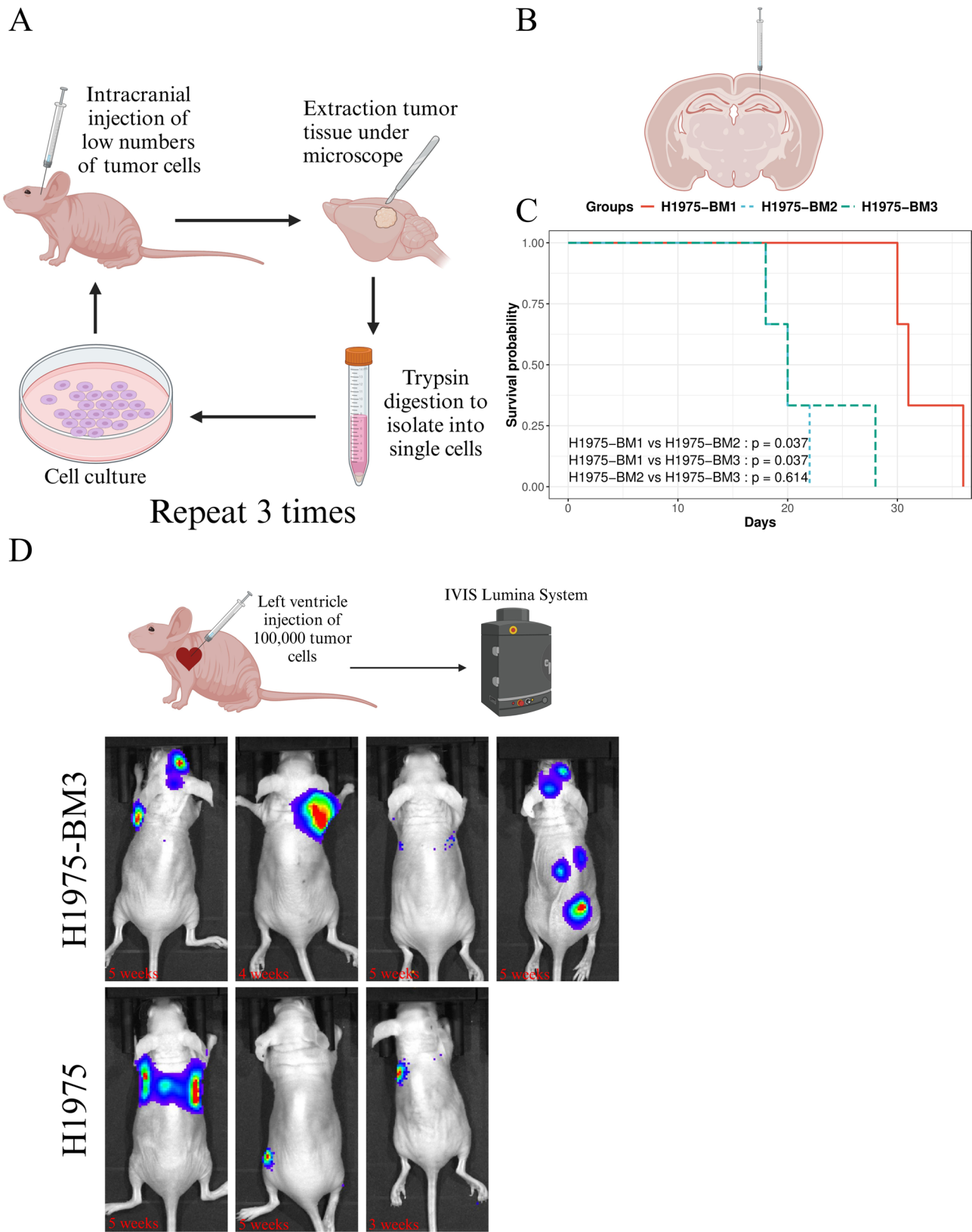
Fig. 1 Intracranial Serial Injection and Brain Metastatic Potential Validation. **A**. Schematic diagram of the overall process for generating BM cell lines. **B**. Diagram of the intracranial injection site. **C**. Kaplan–Meier survival curve of mice. **D**. In vivo imaging showing the tumor growth site in mice, the survival time of mice is marked in the lower left corner

to have reached the study endpoint. After three sequential cycles, we successfully established three BM cell lines: H1975-BM1, H1975-BM2, and H1975-BM3(BM1, BM2 and BM3).

To assess tumor aggressiveness, we injected each BM cell line intracranially into nude mice ($n = 3$ per group) and recorded survival time. Notably, compared to the BM1 group, the BM2 and BM3 groups exhibited significantly shorter survival times. However, no significant difference was observed between BM2 and BM3 (Fig. 1C). These results indicate that after three cycles, the BM3 cell line had acquired sufficient adaptation to the brain microenvironment.

To further verify whether the BM3 cell line possesses true brain metastatic potential, we injected H1975 and BM3 cells into the left ventricle of nude mice and monitored tumor progression using in vivo imaging. The results showed that 50% of mice in the BM3 group developed brain metastases, whereas no brain metastases were observed in the H1975 group (Fig. 1D). This finding suggests that the BM3 cell line not only adapts to the brain microenvironment but also exhibits a strong tropism for brain colonization.

Phenotypic evolution of BM-LUAD cell lines

To investigate the phenotypic changes occurring during brain metastasis, we conducted in vitro experiments for validation. First, we assessed the migration ability of different cell lines at various stages. Interestingly, we found that BM1, an early-stage brain metastatic cell line, exhibited the highest migration capacity, whereas BM3 had the weakest migration ability, even lower than the parental H1975 cells (Fig. 2A). However, in the cell adhesion assay, BM3 formed significantly larger cell clusters compared to other cell lines. From H1975 to BM3, cell adhesion capacity markedly increased (Fig. 2B, C), suggesting that BM3 cells are more prone to forming tumor cell clusters. Recent studies indicate that circulating tumor cell clusters resist mechanical shear and immune attacks and form metastases more efficiently than single cells [1, 11]. Our results therefore suggest that BM3 cells have an enhanced ability for distant metastasis.

Additionally, we examined the proliferation rates of different cell lines (Fig. 2D). The results showed that the parental H1975 cells had the highest proliferation rate, followed by BM1, while BM2 and BM3 exhibited significantly lower proliferation abilities compared to H1975. This suggests that, under in vitro conditions, brain metastatic cell lines proliferate more slowly than the parental cells.

Our in vitro tests showed unexpected results. Although BM2 and BM3 cells had lower migration and proliferation in culture, mice injected intracranially with these cells had significantly shorter survival times. This discrepancy may arise from in vitro conditions that lack cell interactions, variable nutrients, and oxygen gradients, which are present in vivo.

To further explore the phenotypic traits of BM cell lines, we performed subcutaneous injections of BM1 and BM3 cells into nude mice, with 120,000 cells per injection. After 21 days, mice were anesthetized and sacrificed, and tumor tissues were collected (Fig. 3A). The subcutaneous tumors formed oval-shaped masses with a well-defined capsule. Inside the capsule, both solid tumor tissue and tumor secretions were observed (Fig. 3B). Under light examination, the solid tumor tissue also appeared as an oval-shaped mass, allowing measurement without disrupting the capsule (Fig. 3C). Statistical analysis revealed that, compared to the BM1 group, the BM3 group exhibited significantly larger capsule volumes and increased secretory fluid within the capsule (Fig. 3D). Although the mean tumor volume in the BM3 group was higher than in the BM1 group, the difference was not statistically significant, likely due to measurement challenges without disrupting the capsule or the limited sample size.

Overall, integrating both in vitro and in vivo findings, we conclude that as BM3 cells adapt better to the brain microenvironment, they exhibit enhanced secretory activity and cell-cell adhesion. Furthermore, under in vivo conditions, BM3 demonstrates a greater proliferation ability than the early-stage brain metastatic BM1 cells.

Validation of similarity with clinical samples

In previous studies, researchers have established BM cell lines derived from various primary tumors. However, evaluating the actual similarity between BM cell lines and tumor cells from patients remains a challenging issue. In this study, we designed a novel workflow based on the CIBERSORT deconvolution algorithm to address this problem.

First, we selected the scRNA-seq dataset GSE131907 from the GEO database, retaining only primary LUAD and BM-LUAD samples. Standard scRNA-seq analysis identified 65,794 cells, which were classified into 10 distinct cell types based on marker genes (Fig. 4A, B). We then extracted only the tumor cells (Epithelial and Cycling Epithelial), performed dimensionality reduction and clustering, and identified six tumor cell clusters, designated as Tumor C0-C5 (Fig. 4C).

To assess the distribution preference of cell subpopulations in different sample types, we introduced the Ro/e index (the ratio of observed to expected cell numbers). The analysis revealed that Tumor C0, Tumor C1, and Tumor C3 were significantly enriched in BM samples, indicating that these subpopulations are BM-specific tumor cells (Fig. 4D).
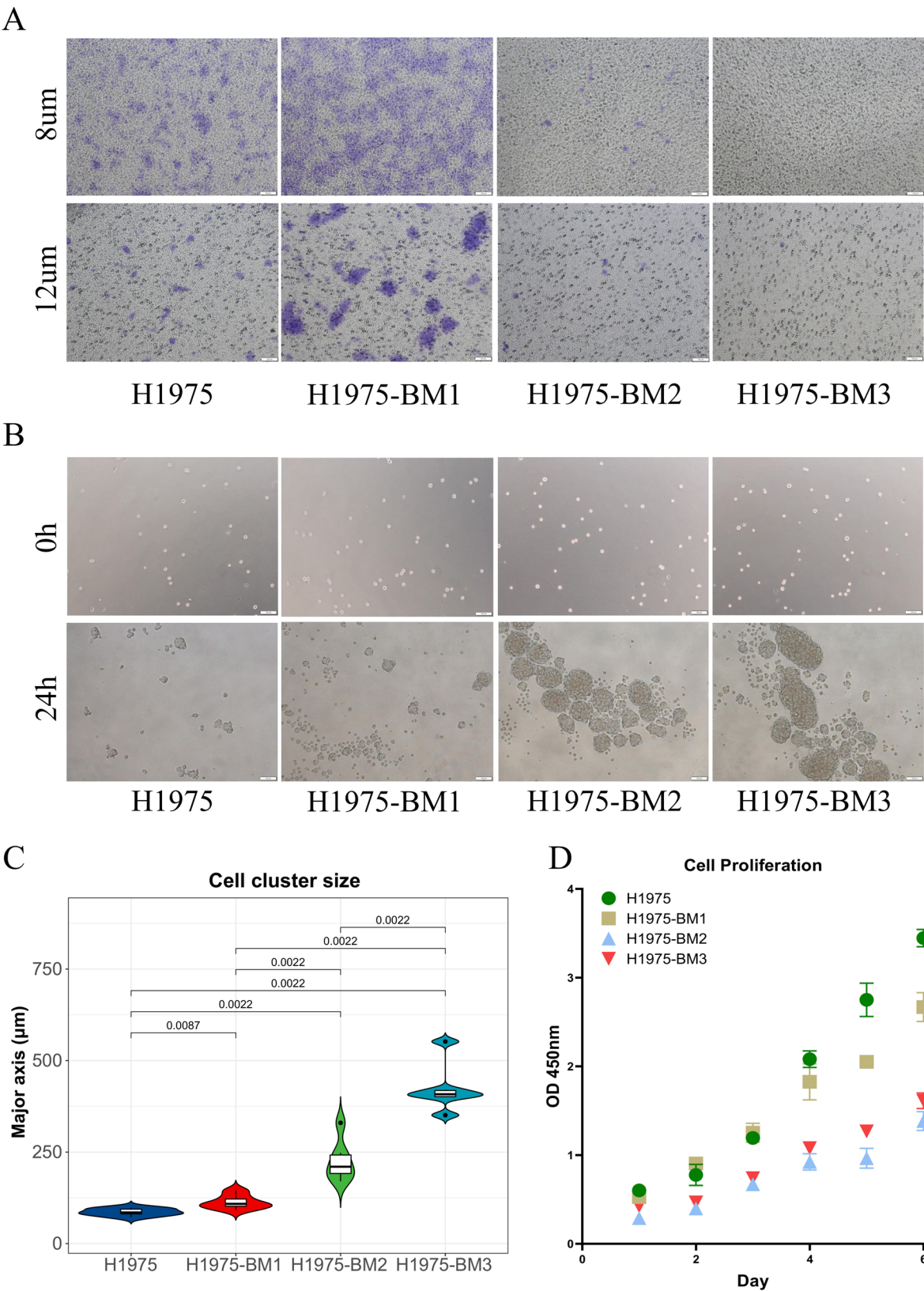
Fig. 2 Phenotypic Differences of BM Cell Lines under In Vitro Conditions. **A**. Cell migration assay; cells that crossed the membrane were stained with crystal violet (scale bar: 100 µm) **B** & **C**. Cell adhesion assay; the major axis of cell clusters was measured and statistically compared. p-values are indicated (scale bar: 100 µm). **D**. Cell proliferation assay.
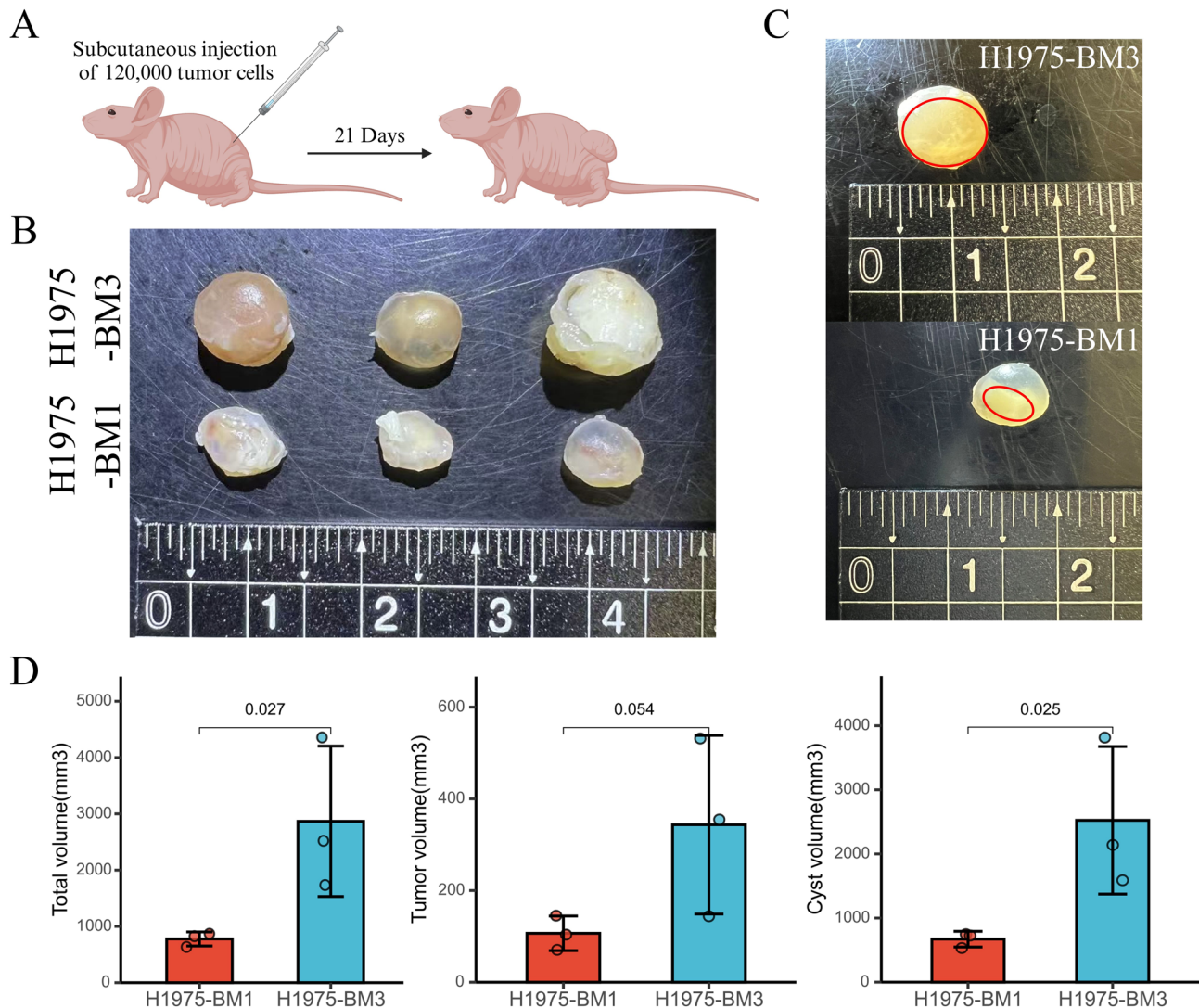
Fig. 3 Subcutaneous Tumor Xenograft Experiments Reveal Phenotypic Differences between BM1 and BM3 Cell Lines. **A**. Schematic diagram of the subcutaneous tumor xenograft workflow. **B**. Appearance of the tumor samples. **C**. Measurement and calculation of both overall volume and solid tumor volume. **D**. Statistical significance of the differences between groups is shown (p-values indicated)

To validate the similarity between the BM cell line and real BM tumor cells, we calculated cell fractions using a deconvolution algorithm (Fig. 4E). The results showed that as the BM cell line advanced, the proportions of Tumor C0 and Tumor C1 steadily increased (Fig. 4F).

Unexpectedly, Tumor C3 was absent in both the parental and BM cell lines, suggesting that this subpopulation is unique to clinical samples. To explore its potential significance, we examined the top 50 marker genes of Tumor C3 and found associations with hypoxia (VEGFA, HILPDA), angiogenesis (VEGFA, GAS6, TNNC1), metabolism (ACADVL, HILPDA, FLCN, TNNC1), and immune regulation (GAS6, PILRB, PNISR) (Fig. 4G). These functions are closely related to the brain microenvironment, including local oxygen pressure, metabolic abnormalities, and tumor microenvironment interactions. Considering

the limitations of in vitro cultures, it is nearly impossible to fully capture these tumor cell characteristics under standard culture conditions.

In summary, our newly designed workflow provides a convenient approach to establish a link between BM cell lines and actual patient samples, allowing us to evaluate their transcriptomic similarities. Our analysis confirms that despite certain objective constraints, the BM cell lines we generated exhibit a high degree of similarity to tumor cells in clinical samples.

Identification of specific transcriptomic modules in BM cell lines

Unsupervised hierarchical clustering analysis and principal component analysis (PCA) grouped BM cell lines at different stages into distinct clusters (Fig. 5A, B).

Fig. 4 (See legend on next page.)
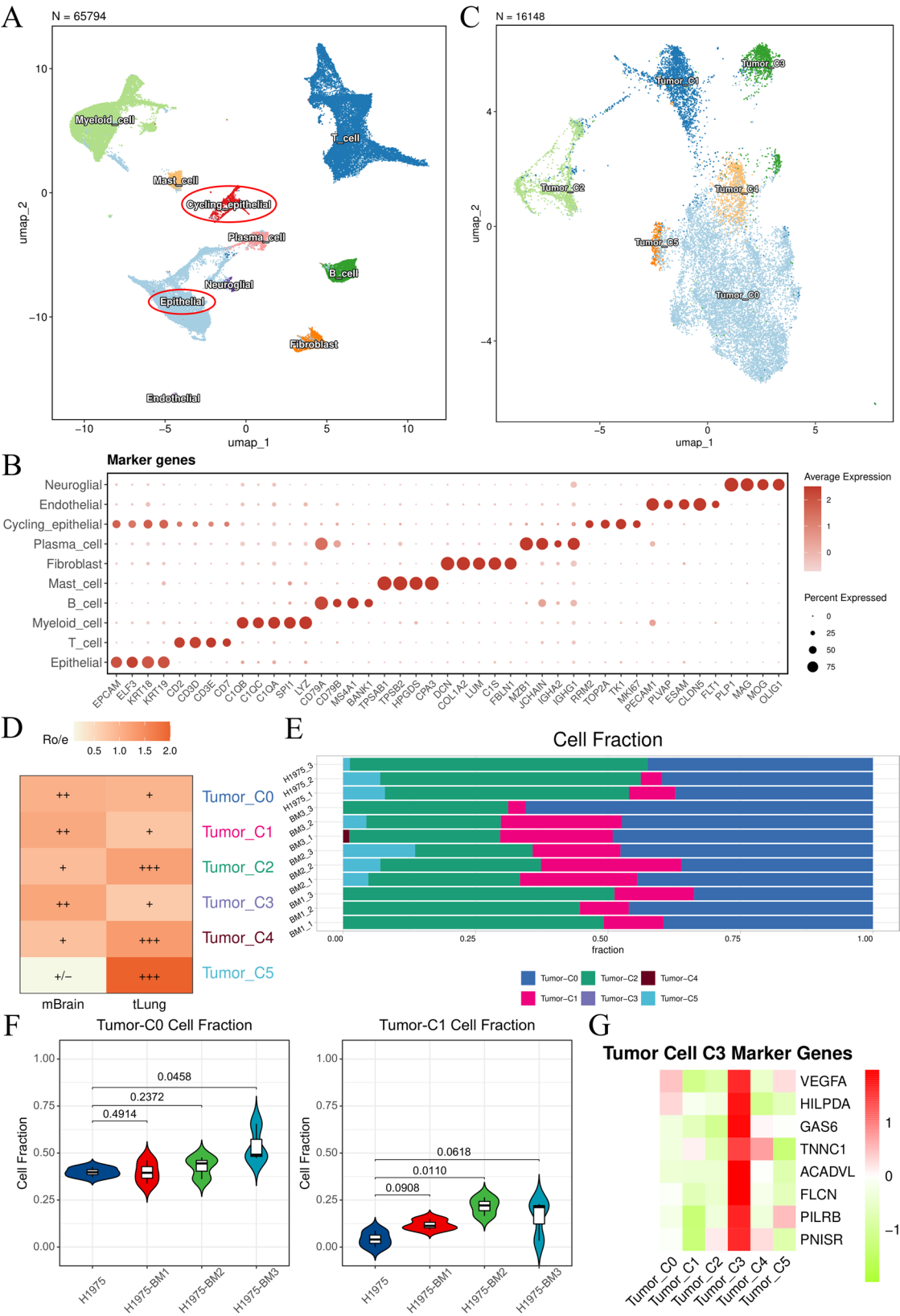
(See figure on previous page.)

Fig. 4 Validation of Similarity with Clinical Samples. **A**. Dimensionality reduction and clustering annotated 10 distinct cell types. **B**. Display of marker genes for different cell types. **C**. Reanalysis of tumor cells (circled in red in A) revealed that they can be divided into six subgroups. **D**. The Ro/e index was calculated to assess the distribution bias of tumor cell subgroups between BM-LUAD samples (mBrain) and primary LUAD samples (tLung). +++ for Ro/e > 1.2; ++ for 1 < Ro/e ≤ 1.2; + for 0.6 ≤ Ro/e ≤ 1; +/− for 0 < Ro/e < 0.6 **E**. Proportions of tumor cell subgroups in the BM cell line samples. **F**. Statistical analysis of the BM-specific subgroups cell fraction; p-values are provided. **G**. Display of key marker genes in the tumor cell C3 subgroup

Interestingly, these clustering results showed that BM1 cells still shared some similarity with the parental H1975 cells, whereas BM2 and BM3 cells formed a separate cluster. Similarly, PCA analysis revealed that H1975 and BM1 were the closest in distance, while BM2 and BM3 were most similar to each other. These findings suggest a significant difference between BM1 and BM3, while BM2 and BM3 share more similarities. This result further supports the reliability of the mouse survival data (Fig. 1C).

Since BM cell lines represent a dynamic evolutionary process, we reasoned that traditional differential expression analysis alone would be insufficient to capture their key characteristics. To better understand gene co-expression patterns at the systems level, we performed weighted gene co-expression network analysis (WGCNA). This unsupervised and unbiased approach identified distinct modules of co-regulated genes (Fig. 5C). Each module, representing a set of co-expressed genes, was assigned a unique color. We then identified the module most positively correlated with each cell line, as these modules contain system-level signature genes (Fig. 5D). Gene ontology (GO) enrichment analysis was performed on each module, and the top eight enriched biological processes were displayed (Fig. 5E).

In BM1 cells, pathways related to glandular structure development (e.g., salivary gland morphogenesis, salivary gland development, exocrine system development) were enriched, suggesting that BM1 cells may reactivate developmental gene programs commonly involved in embryonic or organ development. This "developmental reprogramming" may enhance their differentiation plasticity and adaptability to the microenvironment. In addition, BM1 cells showed enrichment in extracellular matrix (ECM) and structural organization pathways (collagen fibril organization, extracellular matrix organization, extracellular structure organization, external encapsulating structure organization), indicating significant ECM remodeling, a process frequently associated with high cancer invasiveness. This observation aligns with previous phenotypic findings showing that BM1 cells exhibit the highest migratory ability (Fig. 2A). Moreover, the canonical Wnt signaling pathway was specifically enriched in BM1 cells. Since Wnt signaling plays a key role in cell fate determination and stemness maintenance, its activation suggests that BM1 cells may acquire stem-like tumor properties, further enhancing their adaptability and metastatic potential.

In BM3 cells, pathways related to chemotaxis and directional migration (chemotaxis/taxis, cell chemotaxis, leukocyte migration, myeloid leukocyte migration) were significantly enriched. This suggests that BM3 cells activate immune cell-like migratory programs, potentially enhancing their ability to metastasize over long distances. Additionally, cell adhesion-related pathways (cell-matrix adhesion, cell-substrate adhesion) were specifically enriched in BM3 cells, consistent with the observation that BM3 cells form larger tumor cell clusters (Fig. 2B, C), supporting their increased potential for distant metastasis. Importantly, we also observed enrichment of inflammation-related pathways (response to molecule of bacterial origin), suggesting a complex interaction between BM3 cells and the local immune environment. This may involve local inflammation, cytokine secretion, and immune cell recruitment, which could promote tumor growth and immune evasion. The enhanced secretory activity of BM3 cells may play a central role in this process, further explaining why BM3 tumors developed larger secretory cavities in the subcutaneous tumor model (Fig. 3).

In contrast, all pathways enriched in BM2 cells were related to transcriptional regulation and metabolism, suggesting that BM2 represents an intermediate state between early and advanced stages of brain metastasis progression.

Through integrative transcriptomic analysis and experimental validation, we successfully identified distinct molecular characteristics of BM cell lines at different stages. These findings confirm that the BM cell lines generated in this study reliably reflect key molecular features of brain metastases, demonstrating their high validity for further research.

Key hub genes in the gene network

These stage-specific modules represent core gene networks operating in different BM cell lines (Fig. 6A, B). In the H1975 parental cell line, the turquoise module contained 4,913 genes, whereas in the BM1 and BM3 cell lines, the brown and greenyellow modules included 997 and 788 genes, respectively (Fig. 6B). We then visualized the gene networks and identified the top 10 hub genes in each module based on their high KME (eigengene connectivity) values (Fig. 6C). Next, we validated the 10 hub genes identified in the BM3 cell line using transcriptomic data from LUAD and normal lung tissue samples in the TCGA database. Among these genes, six were
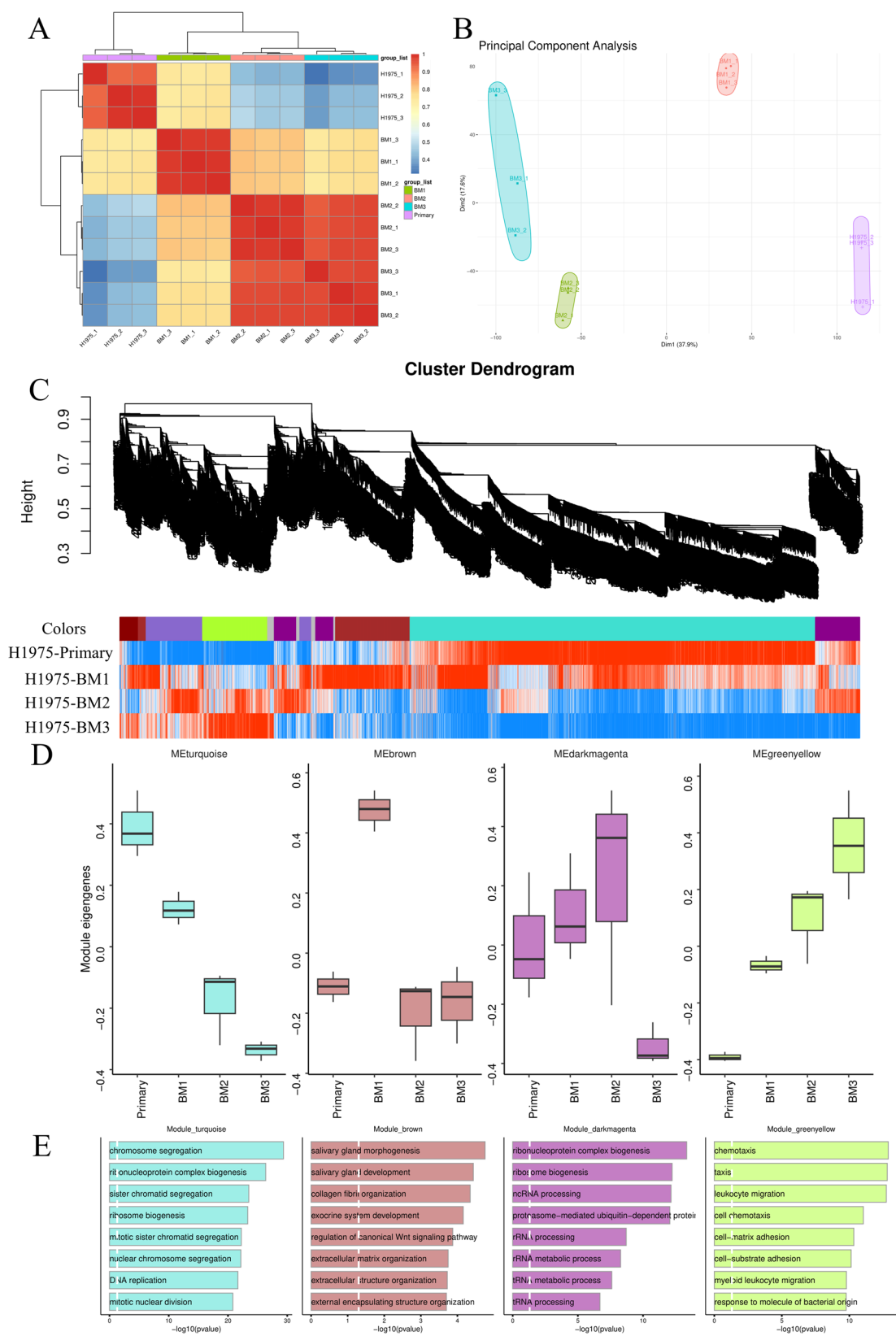
Fig. 5 (See legend on next page.)

(See figure on previous page.)

Fig. 5 Identification of Specific Transcriptomic Modules in BM Cell Lines. **A**. A clustered heatmap displays the correlation among BM cell line samples. **B**. Principal component analysis of all BM cell line samples, with samples from the same cell line highlighted in the same color. **C**. The hierarchical clustering tree depicts co-expression modules identified using WGCNA. Each branch represents a module and is labeled with a color, as shown in the first color band beneath the tree. The additional color bands indicate transcripts that are highly correlated (red) or anti-correlated (blue) in the BM cell lines. **D**. Box plots present the distribution of module correlations across different BM cell lines. **E**. A bar chart shows the top eight representative gene ontology terms enriched in the specific module, with the horizontal axis representing significance

significantly upregulated, while three were significantly downregulated in LUAD samples.

For further verification, we analyzed public proteomic data (ProteomeXchange: PXD027259) from primary LUAD and BM-LUAD samples. Among the 10 hub genes, only four were detected at the protein level. Notably, INPP5D was significantly downregulated in BM-LUAD samples, whereas RAB25 remained significantly upregulated. This suggests that RAB25 may play a crucial role in BM progression of LUAD, warranting further investigation in future studies.

Discussion

In recent years, an increasing number of researchers have focused on BM, highlighting the importance of BM cell lines as fundamental tools for related studies. However, establishing reliable BM cell lines remains an ongoing challenge.

Most studies follow two main approaches to generate BM cell lines. The first involves left ventricular or carotid artery injection [33], which is considered a reliable method but requires a long experimental cycle, higher costs, and specialized imaging equipment. Due to these limitations, this approach is difficult to implement widely. The second, more common method is intracranial injection, which overcomes the drawbacks of the first approach but has some limitations regarding the reliability of BM cell lines. We believe this issue arises from the number of tumor cells injected. Previous studies have typically injected over 50,000 tumor cells [10, 19, 25], whereas, in the early stages of BM, only a few dozen to a few hundred tumor cells successfully colonize the brain environment [2]. Direct intracranial injection of a large number of tumor cells may create an unnatural local advantage, bypassing the adaptation process to the brain environment and compromising the reliability of BM cell lines.

To address these limitations, we developed an improved method using low-cell-number serial intracranial injections to establish BM-LUAD cell lines. Compared to previous studies, we also designed a novel workflow to assess the similarity between BM cell lines and tumor cells from BM-LUAD patient samples. While certain features are difficult to capture in vitro due to inherent culture constraints, we found that with iterative cell line development, the similarity between BM cell lines and

patient-derived BM tumor cells significantly increased. This supports the reliability of our BM cell lines.

Compared to the parental cell line, BM1 cells grow in a brain environment that is entirely different from the lung. To adapt to this new microenvironment, tumor cells must undergo changes. Our findings suggest that BM1 cells acquire stem-like properties through activation of the Wnt signaling pathway, regain differentiation potential by reactivating glandular developmental regulatory networks (leading to intratumoral heterogeneity), and remodel the ECM to enhance their migratory capacity for nutrient acquisition. These characteristics align closely with observations of early-stage BM progression [21, 30], indicating that BM1 is a reliable model for studying early BM development.

In contrast, BM3 cells exhibit different characteristics. Notably, BM3 cells show reduced migration ability, suggesting a higher adaptation to the brain environment [34]. Previous studies have shown that during early metastasis, epithelial tumor cells must undergo epithelial-to-mesenchymal transition (EMT) to invade distant tissues and form metastatic colonies. However, after successful colonization, tumor cells may revert to an epithelial phenotype (mesenchymal-to-epithelial transition, MET), stabilizing their proliferative state while decreasing their migratory and invasive capabilities [21, 30]. This phenomenon may explain why many brain metastases tend to form distinct, well-demarcated tumor masses rather than exhibiting strong invasiveness. Notably, clinical BM-LUAD samples have shown a significant downregulation of key EMT pathway proteins compared to primary LUAD [35], further supporting that BM3 cells represent a more advanced stage of BM progression.

Interestingly, we observed that BM3 cells exhibit enhanced cell-cell adhesion and demonstrate a greater tendency to form clusters. Previous studies have confirmed that circulating tumor cell (CTC) clusters possess higher metastatic potential by altering DNA methylation to facilitate metastatic site establishment, whereas single CTCs exhibit lower survival and metastatic capacity [1, 11]. Stronger adhesion also enhances tumor cell interactions with vascular endothelial cells, promoting blood-brain barrier (BBB) penetration [17, 28, 41]. Additionally, transcriptomic analysis revealed enrichment of signaling pathways related to chemotaxis and inflammatory responses, consistent with in vivo mouse experiments. These findings indicate that despite using intracranial injection, BM3 cells
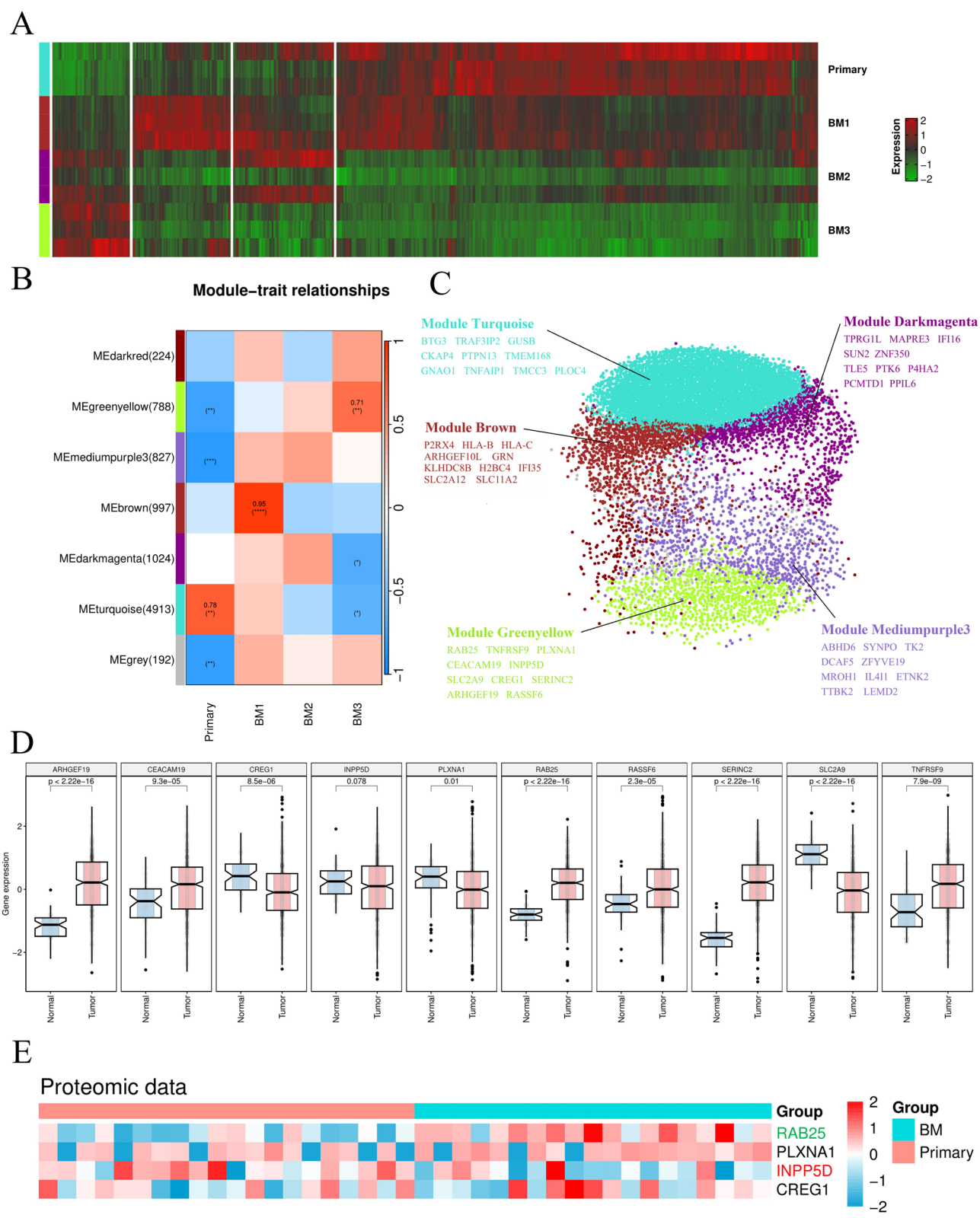
Fig. 6 (See legend on next page.)

(See figure on previous page.)
Fig. 6 Key Hub Genes in the Gene Network. **A**. A heatmap shows the gene expression patterns of the modules with the highest correlation across different cell lines. **B**. All modules are displayed and statistically tested; the turquoise module is significantly associated with the parental cell line, the brown module with the BM1 cell line, and the greenyellow module with the BM3 cell line, while the BM2 cell line lacks any statistically significant modules. *: $0.01 < p < 0.05$; **: $0.001 < p \leq 0.01$; ***: $0.0001 < p \leq 0.001$; ****: $p \leq 0.0001$. **C**. A gene expression network was constructed based on the correlations among all genes in the module, and the top 10 hub genes were identified. **D**. The top 10 hub genes from the BM3-specific greenyellow module were extracted, and their expression in tumor tissue versus normal lung tissue was examined using TCGA-LUAD data, with p-values provided. **E**. Protein expression corresponding to the hub genes was assessed using proteomic data (ProteomeXchange: PXD027259); INPP5D is significantly overexpressed in primary LUAD, while RAB25 is significantly overexpressed in BM-LUAD

retain the ability to target the brain environment and interact with immune cells in the tumor microenvironment.

It is worth noting that, in recent years, many studies have utilized spontaneous tumor mouse models. In the context of EGFR-mutant LUAD research, spontaneous tumor models carrying EGFR-L858R or EGFR-Del19 mutations are commonly employed [15, 24, 26]. Genetically engineered animal models can closely mimic the natural initiation and progression of human LUAD, making them appropriate for investigating the tumor microenvironment, immune responses, and for new drug screening. However, such models also have limitations—for example, tumor development typically requires several weeks to months, and there can be considerable variability in tumor incidence and growth rates among individual mice. In addition, the high cost of these experiments is a major concern. As a result, spontaneous tumor mouse models are rarely used in metastasis research.

Nevertheless, in our planned future studies, genetically engineered animal models may play a more prominent role in brain metastasis research. Specifically, we plan to perform whole-exome sequencing on our BM cell lines to identify significantly mutated genes that arise during cell line evolution. We will then construct mouse models with combined gene mutations to discover novel mutation sites associated with brain metastasis, with the aim of generating spontaneous tumor mouse models that specifically develop brain metastases.

Furthermore, we integrated transcriptomic and proteomic data, identifying RAB25 as a novel potential research target from the core gene network of BM3 cells. Previous studies have shown that high RAB25 expression reduces chemotherapy sensitivity in non-small cell lung cancer [20] and promotes erlotinib resistance via activation of the β1-integrin/AKT/β-catenin pathway [32]. In LUAD, RAB25-mediated EGFR recycling contributes to radiotherapy resistance [40]. However, its specific role in BM-LUAD remains largely unexplored, warranting further investigation. This finding underscores the significance of our improved BM cell lines in advancing research on BM development and progression.

Limitations
The occurrence and progression of brain metastasis is a complex and dynamic process. Although our established BM cell line successfully recapitulates key phenotypes

of brain metastatic tumor cells, the intracranial injection approach primarily models the behavior of tumor cells after colonization in the brain microenvironment. As a result, this method does not fully reflect the characteristics of tumor cells during hematogenous spread or the process of crossing the blood–brain barrier. In future studies, isotope tracing technology may help address this limitation. Additionally, since the primary aim of this research was to establish an accessible and cost-effective method for generating BM cell lines in a standard laboratory setting, we did not perform detailed functional analysis of RAB25. In our future work, we plan to further investigate the role and underlying mechanisms of RAB25 in the progression of brain metastasis.

Conclusion
In this study, we improved the existing classical methods and developed a novel approach to establish BM-LUAD cell lines. Additionally, we designed a new workflow based on the CIBERSORT deconvolution algorithm to compare BM cell lines with patient-derived tumor cells, demonstrating their similarity. Furthermore, transcriptomic analysis and phenotypic experiments revealed distinct characteristics at different stages of BM progression, confirming the reliability of our BM cell lines and their significance for future research.

Abbreviations
LUAD   Lung adenocarcinoma
BM   Brain metastasis
EGFR   Epidermal growth factor receptor
TPM   Transcripts per kilobase million
GO   Gene ontology
ECM   Extracellular matrix
TCGA   The cancer genome atlas
EMT   Epithelial-to-mesenchymal transition
MET   Mesenchymal-to-epithelial transition
CTC   Circulating tumor cell
BBB   Blood-brain barrier

Author contributions
Jintao He, Zen-ichi Tanei, Lei Wang, Masumi Tsuda and Shinya Tanaka designed the study. Jintao He, Zen-ichi Tanei and Yoshitaka Oda performed the mouse experiments. Jintao He, Zen-ichi Tanei and Dao-Sian Wu performed the cell lines experiments. Jintao He obtained RNA bulk sequencing and performed the analysis. All authors reviewed the manuscript.

Declarations

Ethics approval and consent to participate
All animal experiments were conducted in compliance with the guidelines of Hokkaido University Manual for Implementing Animal Experimentation with the approval (No. 17–0061, 22–0089) of Institutional Animal Care and Use Committee at Hokkaido University, Sapporo, Japan.

Consent for publication
Not applicable.

Competing interests
The authors declare no competing interests.

References

1. Aceto N, Bardia A, Miyamoto DT, Donaldson MC, Wittner BS, Spencer JA, Yu M, Pely A, Engstrom A Zhu H (2014) Circulating tumor cell clusters are oligoclonal precursors of breast cancer metastasis. Cell 158: 1110–1122 https://doi.org/10.1016/j.cell.2014.07.013
2. Achrol AS, Rennert RC, Anders C, Soffietti R, Ahluwalia MS, Nayak L, Peters S, Arvold ND, Harsh GR, Steeg PS et al (2019) Brain metastases. Nat Rev Dis Primers 5: 5 https://doi.org/10.1038/s41572-018-0055-y
3. Baran Y, Bercovich A, Sebe-Pedros A, Lubling Y, Giladi A, Chomsky E, Meir Z, Hoichman M, Lifshitz A, Tanay A (2019) MetaCell: analysis of single-cell RNA-seq data using K-nn graph partitions. Genome Biol 20:206. https://doi.org/10.1186/s13059-019-1812-2
4. Bray F, Laversanne M, Sung H, Ferlay J, Siegel RL, Soerjomataram I, Jemal A (2024) Global cancer statistics 2022: GLOBOCAN estimates of incidence and mortality worldwide for 36 cancers in 185 countries. CA Cancer J Clin 74:229–263. https://doi.org/10.3322/caac.21834
5. Chen S (2023) Ultrafast one-pass FASTQ data preprocessing, quality control, and deduplication using Fastp. Imeta 2:e107. https://doi.org/10.1002/imt2.107
6. Cohen M, Giladi A, Gorki AD, Solodkin DG, Zada M, Hladik A, Miklosi A, Salame TM, Halpern KB, David Eet al et al (2018) Lung single-cell signaling interaction map reveals basophil role in macrophage imprinting. Cell 175: 1031–1044 e1018 https://doi.org/10.1016/j.cell.2018.09.009
7. Dai M, Pei X, Wang XJ (2022) Accurate and fast cell marker gene identification with COSG. Brief Bioinform 23. https://doi.org/10.1093/bib/bbab579
8. Duan H, Ren J, Wei S, Yang Z, Li C, Wang Z, Li M, Wei Z, Liu Y, Wang X al (2024) Integrated analyses of multi-omic data derived from paired primary lung cancer and brain metastasis reveal the metabolic vulnerability as a novel therapeutic target. Genome Med 16:138. https://doi.org/10.1186/s13073-024-01410-8
9. Ge M, Zhuang Y, Zhou X, Huang R, Liang X, Zhan Q (2017) High probability and frequency of EGFR mutations in non-small cell lung cancer with brain metastases. J Neurooncol 135:413–418. https://doi.org/10.1007/s11060-017-2590-x
10. Geisler JA, Spehar JM, Steck SA, Bratasz A, Shakya R, Powell K, Sizemore GM (2020) Modeling brain metastases through intracranial injection and magnetic resonance imaging. J Vis Exp: Doi. https://doi.org/10.3791/61272
11. Gkountela S, Castro-Giner F, Szczerba BM, Vetter M, Landin J, Scherrer R, Krol I, Scheidmann MC, Beisel C, Stirnimann CUet al et al (2019) Circulating tumor cell clustering shapes dna methylation to enable metastasis seeding. Cell 176: 98–112 e114 https://doi.org/10.1016/j.cell.2018.11.046
12. Hao Y, Stuart T, Kowalski MH, Choudhary S, Hoffman P, Hartman A, Srivastava A, Molla G, Madad S, Fernandez-Granda Cet al et al (2024) Dictionary learning for integrative, multimodal and scalable single-cell analysis. Nat Biotechnol 42:293–304. https://doi.org/10.1038/s41587-023-01767-y

13. Kienzler JC, Contreras EM, Treger J, Liau LM, Owens GC, Prins RM (2025) Transcriptome analysis of novel B16 melanoma metastatic variants generated by serial intracarotid artery injection. Acta Neuropathol Commun 13:10. https://doi.org/10.1186/s40478-025-01924-1
14. Kim N, Kim HK, Lee K, Hong Y, Cho JH, Choi JW, Lee JI, Suh YL, Ku BM Eum HH (2020) Single-cell RNA sequencing demonstrates the molecular and cellular reprogramming of metastatic lung adenocarcinoma. Nat Commun 11: 2285 https://doi.org/10.1038/s41467-020-16164-1
15. Kwon MC, Berns A (2013) Mouse models for lung cancer. Mol Oncol 7:165–177. https://doi.org/10.1016/j.molonc.2013.02.010
16. Langfelder P, Horvath S (2008) WGCNA: an R package for weighted correlation network analysis. BMC Bioinformatics 9:559. https://doi.org/10.1186/1471-2105-9-559
17. Li Y, Liu F, Cai Q, Deng L, Ouyang Q, Zhang XH, Zheng J (2025) Invasion and metastasis in cancer: molecular insights and therapeutic targets. Signal Transduct Target Ther 10:57. https://doi.org/10.1038/s41392-025-02148-4
18. Lin CW, Huang KY, Lin CH, Hou MH, Lin SH (2025) Diverse clinical outcomes for the EGFR–mutated and ALK–rearranged advanced non–squamous non–small cell lung cancer. Oncol Lett 29:125. https://doi.org/10.3892/ol.2025.14872
19. Liu X, Liu S, Yang Y, Cai H, Zheng R, Zhang Y, Li X, Fan F, Liu H, Li S (2024) Animal models of brain and spinal cord metastases of NSCLC established using a brain stereotactic instrument. Heliyon 10:e24809. https://doi.org/10.1016/j.heliyon.2024.e24809
20. Ma YF, Yang B, Li J, Zhang T, Guo JT, Chen L, Li M, Chu J, Liang CY, Liu Y (2015) Expression of Ras-related protein 25 predicts chemotherapy resistance and prognosis in advanced non-small cell lung cancer. Genet Mol Res 14:13998–14008. https://doi.org/10.4238/2015.October.29.19
21. Massague J, Obenauf AC (2016) Metastatic colonization by Circulating tumour cells. Nature 529:298–306. https://doi.org/10.1038/nature17038
22. Newman AM, Liu CL, Green MR, Gentles AJ, Feng W, Xu Y, Hoang CD, Diehn M, Alizadeh AA (2015) Robust enumeration of cell subsets from tissue expression profiles. Nat Methods 12:453–457. https://doi.org/10.1038/nmeth.3337
23. Patro R, Duggal G, Love MI, Irizarry RA, Kingsford C (2017) Salmon provides fast and bias-aware quantification of transcript expression. Nat Methods 14:417–419. https://doi.org/10.1038/nmeth.4197
24. Politi K, Zakowski MF, Fan PD, Schonfeld EA, Pao W, Varmus HE (2006) Lung adenocarcinomas induced in mice by mutant EGF receptors found in human lung cancers respond to a tyrosine kinase inhibitor or to down-regulation of the receptors. Genes Dev 20:1496–1510. https://doi.org/10.1101/gad.1417406
25. Qu F, Brough SC, Michno W, Madubata CJ, Hartmann GG, Puno A, Drainas AP, Bhattacharya D, Tomasich E, Lee MC al (2023) Crosstalk between small-cell lung cancer cells and astrocytes mimics brain development to promote brain metastasis. Nat Cell Biol 25:1506–1519. https://doi.org/10.1038/s41556-023-01241-6
26. Regales L, Gong Y, Shen R, de Stanchina E, Vivanco I, Goel A, Koutcher JA, Spassova M, Ouerfelli O, Mellinghoff IK et al (2009) Dual targeting of EGFR can overcome a major drug resistance mutation in mouse models of EGFR mutant lung cancer. J Clin Invest 119: 3000–3010 https://doi.org/10.1172/JCI38746
27. Shi W, Tanzhu G, Chen L, Ning J, Wang H, Xiao G, Peng H, Jing D, Liang H Nie J (2024) radiotherapy in preclinical models of brain metastases: A review and recommendations for future studies. Int J Biol Sci 20: 765–783 https://doi.org/10.7150/ijbs.91295
28. Soto MS, Serres S, Anthony DC, Sibson NR (2014) Functional role of endothelial adhesion molecules in the early stages of brain metastasis. Neuro Oncol 16:540–551. https://doi.org/10.1093/neuonc/not222
29. Sperduto PW, De B, Li J, Carpenter D, Kirkpatrick J, Milligan M, Shih HA, Kutuk T, Kotecha R, Higaki Het al et al (2022) Graded prognostic assessment (GPA) for patients with lung Cancer and brain metastases: initial report of the small cell lung Cancer GPA and update of the Non-Small cell lung Cancer GPA including the effect of programmed death ligand 1 and other prognostic factors. Int J Radiat Oncol Biol Phys 114:60–74. https://doi.org/10.1016/j.ijrobp.2022.03.020
30. Tam WL, Weinberg RA (2013) The epigenetics of epithelial-mesenchymal plasticity in cancer. Nat Med 19:1438–1449. https://doi.org/10.1038/nm.3336
31. Villano JL, Durbin EB, Normandeau C, Thakkar JP, Moirangthem V, Davis FG (2015) Incidence of brain metastasis at initial presentation of lung cancer. Neuro Oncol 17:122–128. https://doi.org/10.1093/neuonc/nou099
32. Wang J, Zhou P, Wang X, Yu Y, Zhu G, Zheng L, Xu Z, Li F, You Q, Yang Qet al et al (2019) Rab25 promotes erlotinib resistance by activating the beta1

integrin/AKT/beta-catenin pathway in NSCLC. Cell Prolif 52:e12592. https://doi.org/10.1111/cpr.12592

33. Wang L, Chen X, Dong C, Yin S, Liang L, Zhou A (2024) Protocol for generating brain metastatic tumor cells through repeated intracardiac injections in mice. STAR Protoc 6:103531. https://doi.org/10.1016/j.xpro.2024.103531

34. Wei Q, Qian Y, Yu J, Wong CC (2020) Metabolic rewiring in the promotion of cancer metastasis: mechanisms and therapeutic implications. Oncogene 39:6139–6156. https://doi.org/10.1038/s41388-020-01432-7

35. Woldmar N, Schwendenwein A, Kuras M, Szeitz B, Boettiger K, Tisza A, Laszlo V, Reiniger L, Bago AG, Szallasi Zet al et al (2023) Proteomic analysis of brain metastatic lung adenocarcinoma reveals intertumoral heterogeneity and specific alterations associated with the timing of brain metastases. ESMO Open 8:100741. https://doi.org/10.1016/j.esmoop.2022.100741

36. Xie J, Yang A, Liu Q, Deng X, Lv G, Ou X, Zheng S, Situ MY, Yu Y, Liang JY al (2024) Single-cell RNA sequencing elucidated the landscape of breast cancer brain metastases and identified ILF2 as a potential therapeutic target. Cell Prolif 57:e13697. https://doi.org/10.1111/cpr.13697

37. Xue Z, Huang K, Cai C, Cai L, Jiang CY, Feng Y, Liu Z, Zeng Q, Cheng L, Sun YE al (2013) Genetic programs in human and mouse early embryos revealed by single-cell RNA sequencing. Nature 500:593–597. https://doi.org/10.1038/nature12364

38. Zeng D, Fang Y, Qiu W, Luo P, Wang S, Shen R, Gu W, Huang X, Mao Q, Wang G al (2024) Enhancing immuno-oncology investigations through multidimensional decoding of tumor microenvironment with IOBR 2.0. Cell Rep Methods 4:100910. https://doi.org/10.1016/j.crmeth.2024.100910

39. Zhang L, Yu X, Zheng L, Zhang Y, Li Y, Fang Q, Gao R, Kang B, Zhang Q, Huang JY et al (2018) Lineage tracking reveals dynamic relationships of T cells in colorectal cancer. Nature 564: 268–272 https://doi.org/10.1038/s41586-018-0694-x

40. Zhang L, Xie B, Qiu Y, Jing D, Zhang J, Duan Y, Li Z, Fan M, He J, Qiu Y et al (2020) Rab25-mediated egfr recycling causes tumor acquired radioresistance. iScience 23: 100997 https://doi.org/10.1016/j.isci.2020.100997

41. Zhang B, Li X, Tang K, Xin Y, Hu G, Zheng Y, Li K, Zhang C, Tan Y (2023) Adhesion to the brain endothelium selects breast Cancer cells with brain metastasis potential. Int J Mol Sci 24. https://doi.org/10.3390/ijms24087087

Publisher's note